Supporting information for:

Visualizing Heterogeneous Protein Conformations with Multi-Tilt Nanoparticle-Aided Cryo-Electron Microscopy Sampling

Changin Kim,[1,2,3,‡] *Yeeun Kim,*[4,‡] *Sang Jin Lee,*[1,2,3] *So Ri Yun,*[1,2,3] *Jungkweon Choi,*[1,2,3] *Seong Ok Kim,*[1,2,3] *Yongsoo Yang,*[4,]* *& Hyotcherl Ihee,*[1,2,3,]*

[1]Department of Chemistry, Korea Advanced Institute of Science and Technology (KAIST), Daejeon 34141, Republic of Korea

[2]KI for the BioCentury, Korea Advanced Institute of Science and Technology (KAIST), Daejeon 34141, Republic of Korea

[3]Center for Advanced Reaction Dynamics, Institute for Basic Science (IBS), Daejeon 34141, Republic of Korea

[4]Department of Physics, Korea Advanced Institute of Science and Technology (KAIST), Daejeon 34141, Republic of Korea

‡These authors contributed equally.

Corresponding Authors
*Yongsoo Yang: yongsoo.yang@kaist.ac.kr
*Hyotcherl Ihee: hyotcherl.ihee@kaist.ac.kr

Supporting Notes

Supporting Note S1. A discussion on the discrepancy between the MT-NACS data and those from X-ray crystallography and NMR. The structures determined with X-ray crystallography[1-8] and NMR[9-12] appear to contradict the MT-NACS data. X-ray crystal structures of apo-CaM and holo-CaM indicate that the 2-117 inter-residue distance increases upon Ca^{2+} binding, and the inter-residue distance distributions of holo-CaM structures determined with NMR[9-12] show broader inter-residue distance distributions compared to those of apo-CaM (Table 1 and Figure S3). These discrepancies may be partially attributed to the sample preparation conditions used for measurements (Table 1). For MT-NACS, ensemble FRET[13-16, 18] and smFRET[17, 19-23], the same salt concentration and pH were used before and after Ca^{2+} binding. In contrast, different experimental conditions for apo-CaM and holo-CaM were used for X-ray crystallography[1-8] and NMR[9-12] measurements. The salt concentration and pH for X-ray crystallography measurements[1-8] were 50 mM and 6.5 for apo-CaM, while 5-55 mM and 4-5.6 (relatively low salt concentration and pH) were used for holo-CaM. We note that multiple studies[14, 16, 24-26] reported that the flexibility of the α-helical linker between the N-terminal and C-terminal domains of CaM can be strongly affected by experimental parameters such as salt concentration and pH. Since the linker fluctuations can cause relative reorientation and separation of the lateral domains[14, 16], there is a possibility that the structural changes might have originated from the differences in sample preparation conditions as well as Ca^{2+} binding. Also considering the high sample concentration required for crystallization and the fluorinated solvent in the crystallization buffer promoting the rigid and long α-helical central linker of crystallized holo-CaM[27], one cannot exclude the possibility that the extended conformation of holo-CaM is an artifact from the crystallization condition. For NMR structures[9-12], the pH and

salt concentrations do not show significant differences for apo-CaM and holo-CaM, but the used temperatures show significant differences. The salt concentration and pH were 100 mM and 6.3-7.5 for both apo-CaM and holo-CaM (except for one study[11] which used 0 mM salt concentration for holo-CaM), and the temperatures were 23 and 25 °C for apo-CaM and 32 and 37 °C for holo-CaM. Since the unfolding of CaM becomes accelerated at elevated temperatures[28], the holo-CaM measured at a higher temperature compared to that of apo-CaM can show more flexible structures, resulting in longer residue distances.

Supporting Note S2. Charge screening effect to explain the salt concentration dependence of the inter-domain distance. The salt concentration dependence of the inter-domain distance can be explained in terms of the charge screening effect[39]; the electrostatic repulsion between the N-terminus and C-terminus domain can be more effectively screened in the solution of a larger ionic strength (i.e., higher salt concentration), causing a smaller average interparticle distance in 150 mM NaCl compared to that in 50 mM NaCl. Also, since the negative-charge-induced electrostatic repulsion in holo-CaM is considerably reduced due to the binding of four positive Ca^{2+} ions, varying the charge environment by differing salt concentration causes less effect on the inter-domain distance of holo-CaM. This explains the less pronounced salt concentration dependence for holo-CaM.

Supporting Note S3. Binding characteristics of CaM and Aβ25-35. Before actual MT-NACS measurements, we checked their binding characteristics under our experimental

conditions. Circular dichroism (Figure S1c) spectra and Thioflavin T (ThT) aggregation assay (Figure S2a) showed that the CaM can efficiently inhibit the amyloid fibrils development, and the isothermal titration calorimetry experiment further confirmed the 1:1 binding ratio between the CaM and Aβ25-35 (Supporting Method S3 and Figure S2b).

Supporting Note S4. Limitations of the MT-NACS technique. The MT-NACS technique has several limitations. Firstly, since the mutated protein samples need to be prepared for each target pair, extracting distance distributions for multiple pairs of different sites demands effort proportional to the number of different pairs. Secondly, although our CD spectra confirm that labeling AuNPs to proteins does not induce noticeable perturbation in the secondary structure, the influence of AuNPs on the tertiary structure and its structural dynamics cannot be completely ruled out. Thirdly, although MT-NACS offers the ability to observe significant structural changes based on distance distribution, it does not provide atomic-level resolution as compared to techniques such as X-ray crystallography. Finally, it would be challenging to obtain the distance distribution between a short distance within which two nanoparticles cannot be located without collision.

Supporting Methods

Supporting Method S1. CaM expression and purification. The CaM protein was prepared according to a reported protocol[29]. The bovine CaM gene was cloned into the pET-His6-TEV-LIC cloning vector (2B−T). The mutant with Asp2 and Thr117 residues mutated to cysteine (denoted as 2-117 in the following) was constructed using the EZchange® mutagenesis kit (Enzynomics™, South Korea). CaM wild type (WT) and 2-117 were expressed and purified in the same procedures. CaM was overexpressed in *Escherichia coli* BL21 (DE3) at 37 °C via induction of 0.4 mM IPTG (isopropyl-1-thio-β-D-galactopyranoside). The protein carrying an N–terminal His-tag was purified via Ni Sepharose™ 6 Fast Flow affinity chromatography column (Cytiva, USA). The N-terminal His-tag was removed by incubation with TEV protease during dialysis against 20 mM Tris−HCl, pH 8.0, 50 mM NaCl, and 1 mM DTT. TEV protease was removed by the Ni affinity chromatography step. The protein solution was loaded onto a Q-Sepharose Fast Flow anion exchange chromatography column (Cytiva, USA). Equilibration and elution were performed with 20 mM Tris-HCl, pH 8.0, with a linear salt gradient from 50 mM to 1 M NaCl. The fractions were dialyzed against 20 mM HEPES, pH 6.5 with 150 mM NaCl or 50 mM NaCl and 1 mM EGTA.

Supporting Method S2. AuNPs labeling of CaM. The AuNP labeling of CaM and the purification of AuNP-labeled CaM were carried out as described previously[30]. Before labeling, trace metal contaminations were removed from AuNP solutions (Nanoprobes, USA) to prevent unwanted metal ion binding at the EF-motifs of CaM by the dialysis with 20 mM HEPES, pH 6.5 with 150 mM or 50 mM NaCl. To reduce disulfide bonds, a 10-fold molar excess of tris(2-

carboxyethyl)phosphine hydrochloride (TCEP) was added to 100 μl CaM. After 15 minute incubation at room temperature, a threefold excess of AuNP was mixed with CaM and incubated for 5 hours at room temperature (CaM actual concentration: 20 μM). Uncoupled AuNP or single AuNP conjugated CaM molecules were removed using a size exclusion chromatography (SEC) column (Enrich^{TM} SEC 70 column, Bio-Rad, USA) (Figure S4a). To purify AuNP-labeled apo-CaM samples, 20 mM HEPES at pH 6.5 with 150 mM NaCl (high salt condition) or 50 mM NaCl (low salt condition) was used as SEC buffers, and for AuNP-labeled holo-CaM, the same SEC buffers with 1 mM CaCl$_2$ were used. The absorbance according to the elution volume was measured at two wavelengths (280 nm and 420 nm), and the elution profiles at 280 nm are shown in Figure S4b. The elution profile at 420 nm, where only AuNPs can absorb, can be decomposed into four peaks (Figure S4c). Based on the estimated molecular weights using the Bio-Rad gel-filtration standard (Bio-Rad, USA), the first two peaks can be assigned to CaM labeled with two AuNPs and CaM labeled with one AuNP, while the remaining two peaks are attributed to unlabeled AuNPs. The center portion (0.4 mL) of the elution fraction corresponding to the first peak was used to prepare the cryo-EM samples for the MT-NACS experiment. The concentration of CaM labeled with two AuNPs (0.5 μM) was estimated based on the area of the center portion relative to the entire area including all four peaks. Throughout the rest of this text, the term 'AuNP-labeled CaM' refers specifically to CaM labeled with two AuNPs.

Supporting Method S3. Characterization of CaM and AuNP-labeled CaM with and without Ca²⁺ and Aβ. The purified CaM mutants and AuNP-labeled CaM with and without Ca^{2+} and amyloid β-peptide (Aβ) were characterized by circular dichroism (CD) spectroscopy,

Thioflavin T (ThT) aggregation assay, and isothermal titration calorimetry (ITC) measurement. CD spectra were measured with a JASCO-815 150-L CD spectropolarimeter (JASCO, Japan), to investigate the secondary structure changes of CaM and AuNP-labeled CaM upon binding Ca^{2+} and Aβ25-35 peptide (Figure S1). The aggregation intensities of Aβ, CaM without Aβ, and CaM with Aβ were performed by Thioflavin T (ThT) fluorescence assay (Figure S2a). Briefly, samples containing CaM (20 μM) in the absence and presence of Aβ1-42 (25 μM) (Sigma Aldrich, USA) or Aβ25-35 (25 μM) (Sigma Aldrich, USA) were incubated for 5 hours in 20 mM HEPES, pH 6.5, 150 mM NaCl, at 37 °C. Upon addition of ThT (20 μM), the fluorescence values were acquired with excitation at 440 nm and emission at 490 nm by a fluorescence microplate reader (SpectraMax M5 microplate reader, Molecular Devices, USA). Binding affinities between CaM and Aβ25-35 were measured through isothermal titration calorimetry (ITC200, MicroCal, USA) at room temperature (Figure S2b). Samples of 0.2 mM Aβ25-35 and 0.02 mM CaM were used for titration. Integrated exothermal peaks were fitted to a one-site binding model, and the binding ratio and constants were obtained through the Origin program (OriginLab).

Supporting Method S4. Cryo-EM experiment. AuNP-labeled apo-CaM and AuNP-labeled holo-CaM under high salt (150 mM) and low salt (50 mM) conditions without Aβ25-35 and AuNP-labeled apo-CaM and AuNP-labeled holo-CaM under high salt (150 mM) with Aβ25-35 (25 μM) were used for cryo-EM experiments. The Ca^{2+} concentration was 1 mM, and the concentrations of AuNP-labeled apo-CaM and AuNP-labeled holo-CaM are 0.5 μM. For AuNP-labeled CaM with Aβ25-35, AuNP-labeled CaM was mixed with Aβ25-35 for 10 seconds prior to vitrification. Each of the purified CaM samples labeled with AuNPs (2.5 μl)

was deposited onto a 200-mesh copper Quantifoil R 2/1 grid that had been glow-discharged. The grid was then rapidly plunged into liquid ethane using a vitrification device (FEI VitrobotTM Mark IV, USA). For all samples, the following blotting conditions were used; blot total: 1, blotting force: 5, blot time: 3 s, temperature: 4 °C, and humidity: 100 %. Tilt series were measured at two or three different angles chosen from 0°, 30° and −30°, depending on experimental conditions (dose limit, image contrast, etc.) using two 200 kV Glacios cryo-TEMs (Thermo Fisher Glacios, USA), one (microscope 1) located at KAIST and the other one (microscope 2) located at Institute for Basic Science. The images (4096 × 4096 pixels) were acquired at low dose mode (a total dose of 60 to 240 e⁻ / Å² per tilt series) with a defocus range of −2.0 to 2.0 μm using a Ceta-D camera (Thermo Fisher Scientific, USA) at 120,000 × magnification, corresponding to a pixel size of 0.89 Å. The rotation axes, denoted as **w**, for the two microscopes were calibrated by tracking the positions of a fixed object during the rotation, resulting in $\theta = 0.05°$ and $\varphi = -1.05°$ for microscope 1 and $\theta = 0.04°$, $\varphi = -1.63°$ for microscope 2, where θ represents the angle between the image plane (*x-y* plane) and the rotation axis and φ represents the angle between the *x*-axis and the rotation axis projected on the image plane.

Supporting Method S5. Calculating the interparticle distances of AuNP-labeled proteins.
The process of calculating the 3D interparticle distance between AuNPs labeled on a protein from a cryo-EM tilt series consists of the following three steps (Figure S5): (I) particle locating, (II) particle tracking in tilt series images, and (III) calculating the 3D positions of particles and the interparticle distance. The details of each step are described in the following subsections.

(I) Particle locating. We post-processed the cryo-EM images as follows. To increase the signal-to-noise ratio of the cryo-EM images, we first applied a 4 × 4 binning to the images. Each image was then normalized by dividing it by the maximum pixel value (Figure S6a), followed by contrast inversion (Figure S6b).

To reduce the background noise of the contrast-inverted images, we applied the following procedure. (i) The texture of the background noise was extracted by applying a boxcar convolution (kernel size of 46.28 × 46.28 Å) to the images. (ii) Gaussian smoothing (The standard deviation and kernel size were 3.56 Å and 39.16 × 39.16 Å, respectively.) was applied to the images to remove high-frequency noise. (iii) The boxcar-convoluted images were subtracted from the Gaussian-smoothed images, resulting in images with reduced background noise[31] (Figure S6c).

To obtain the 2D coordinates of the AuNP locations from the post-processed images (Figure S6c), we first applied an intensity threshold (The values were adjusted between 0.005 and 0.01 depending on the contrast of individual images.) to remove low-intensity pixels. Then, local maxima pixels were identified, and their 2D coordinates were recorded in a list. If there were multiple local maxima within a distance of less than 10.68 Å between them, only the brightest pixel among them was kept in the list to ensure that only one local maximum was identified for each AuNP[31].

Some of the identified local maxima originated from background noise, not AuNPs. To remove those from the list, a region of 5 × 5 pixels centered around each local maximum was cropped from the original image (not post-processed), and their average intensity was calculated. If the average intensity was above the intensity threshold (adjusted between 0.25

and 0.6, depending on the image contrast), the local maximum was removed from the list (Figure S6d).

The images often contained contrast from small crystal ice flakes, and several aggregated local maxima were found at the crystal ice boundary (Figure S7a−c). To remove the crystal ice boundary artifacts, we isolated the crystal ice region by applying a Gaussian smoothing (The standard deviation and kernel size were 3.56 Å and 17.8 × 17.8 Å, respectively.) to the original image (before post-processing), followed by intensity thresholding (threshold adjusted between 0.35 and 0.5) to create a binary mask image (The pixels of intensity below the threshold will have the value of 1, and all other pixels will become zero pixels; Figure S7d). Contributions from background intensity fluctuation or AuNP contrasts were removed by applying an area threshold (adjusted between 30 $pixel^2$ to 100 $pixel^2$) to the binary mask image using the MATLAB built-in function 'bwareaopen' (Figure S7e), leaving only the crystal ice region in the mask image. The mask was expanded using the MATLAB built-in function 'imdilate' (Figure S7f) to fully enclose the crystal ice boundary region inside the mask (the structuring element for the dilation was a disk whose radius was adjusted between 5 pixels to 50 pixels), and the 2D coordinates of local maxima within the mask were removed from the list. We manually checked the remaining 12,706 local maxima 2D coordinates within the list and removed 855 of them which were clearly not AuNPs.

The precision of the local maxima 2D coordinates is limited by the pixel size. To achieve sub-pixel precision, we cropped an area of 7 × 7 pixels around each local maximum from the post-processed image and fitted the local intensities using a 2D Gaussian function[32]. If the distance between fitted 2D coordinates and the original 2D coordinates was more than 2 pixels, the intensities were re-fitted using a larger cropped area (11 × 11 pixels). If the distance

was still more than 2 pixels, the fitting was re-tried using a smaller crop size (3×3 pixels). If the distance was still more than 2 pixels, the local maxima pixel was regarded as an unfittable peak and removed the 2D coordinates of that from the list. The 2D coordinates of successfully fitted Gaussian peaks were used as more precise 2D coordinates of the AuNPs.

(II) Particle tracking in tilt series. We developed an algorithm to track the AuNPs viewed from two angles as follows. First, a reference angle θ_1 was selected for a given rotation axis $\mathbf{w}$. Since we have the projected AuNP positions ($x_j(\theta_1)$, $y_j(\theta_1)$) (j represents the located particle index), by having a rough guess of their z positions $z_j(\theta_1)$, we can estimate the projected positions of the particles at the tilt angle of θ_n ($x_{j,calc}(\theta_n)$, $y_{j,calc}(\theta_n)$). By assuming that all particles at θ_1 are in the same plane, the z positions at θ_1 can be estimated according to the following equation.

$$z_j(\theta_1) = d_j(\theta_1)\tan\theta_1 \tag{S1}$$

where $d_j(\theta_1)$ is the distance between the jth particle and the rotation axis projected on the image plane. Then ($x_{j,calc}(\theta_n)$, $y_{j,calc}(\theta_n)$) can be represented using the reference angle positions as:

$$\begin{pmatrix} x_{j,calc}(\theta_n) \\ y_{j,calc}(\theta_n) \end{pmatrix} = \text{Proj}\left(R(\theta_n - \theta_1, \mathbf{w}) \begin{pmatrix} x_j(\theta_1) \\ y_j(\theta_1) \\ z_j(\theta_1) \end{pmatrix} \right) + \begin{pmatrix} X_n \\ Y_n \end{pmatrix} \tag{S2}$$

where $R(\theta_n - \theta_1, \mathbf{w})$ is the three-dimensional rotation matrix for the rotation angle of $\theta_n - \theta_1$ around the rotation axis $\mathbf{w}$, Proj is a matrix that projects the 3D position vectors into the x-y plane, and (X_n, Y_n) is the x-y translational vector applied during the tilt series measurements to keep the target inside the field of view at each tilt angle. To determine the X_n and Y_n, we scanned them in the range of -500 to 500 pixels with a step of 5 pixels. During the scan, we calculated

the distance between the experimentally determined 2D coordinates of the AuNPs at θ_n ($x_k(\theta_n)$, $y_k(\theta_n)$) and the calculated 2D coordinates ($x_{j,calc}(\theta_n)$, $y_{j,calc}(\theta_n)$) for the given (X_n, Y_n) for each j. Then, we searched for the shortest distance (L_j) among the calculated distances. We counted the number of L_js which are smaller than 15 pixels, and picked the (X_n, Y_n) vector which maximizes the number. If two or more (X_n, Y_n) vectors have the same maximum number, we counted the number of L_j which are smaller than 7.5 pixels and picked the one which maximizes the number among them. If there are still more than one (X_n, Y_n) vectors that have the same maximum number, the one with the smallest average L_j was selected. Once the unique (X_n, Y_n) is determined from the coarse scan of 5 pixels step, we re-ran the scan in the range of ± 3 pixels around the (X_n, Y_n) with a step size of 1 pixel to determine the final ($X_{n,final}$, $Y_{n,final}$) which shows the smallest average L_j. After this, ($x_{j,calc}(\theta_n)$, $y_{j,calc}(\theta_n)$) was calculated using the determined ($X_{n,final}$, $Y_{n,final}$) for each j, and by comparing it with the experimentally determined 2D coordinates of AuNPs at θ_n, the one closest to ($x_{j,calc}(\theta_n)$, $y_{j,calc}(\theta_n)$) was identified. The closest AuNP was marked as the same AuNP with the jth AuNP in θ_1, and its 2D coordinates and the distance between ($x_{j,calc}(\theta_n)$, $y_{j,calc}(\theta_n)$) and the 2D coordinates of the closest AuNP were stored in a list of tracked particles. During the tracking process, if two or more AuNPs in θ_1 were marked as the same with a single AuNP at θ_n, only the one (among the particles in θ_1) with the smallest distance to the AuNP at θ_n was selected as the correctly tracked pair. The mistracked particles in θ_1 were paired with the next closest particle in θ_n and recorded again in the list of tracked particles. This process was repeated until the number of one-to-one tracked pairs is equal to the number of particles in θ_1 or that in θ_n, whichever is smaller. The remaining particles were regarded as un-trackable particles, and the 2D coordinates of these particles in θ_1 and θ_n were removed from the list. This two-angle tracking procedure was applied to every possible combination of angle pairs; for tilt series of 3 angles (0°, 30° and −30°), the tracking was

performed for each of three different pairs [(0°, 30°), (0°, −30°) and (30°, −30°)], respectively, with the reference angle of 0° for (0°, 30°) and (0°, −30°) pairs and 30° for the (30°, −30°) pair.

For the tilt series with 3 angles of 0°, 30° and −30°, some particles were visible in all three tilt angles. To identify those, we first applied an 8 nm distance threshold to the tracked particle and corresponding distance list of (0°, 30°) and (0°, −30°) pairs to remove the pairs which move unphysically large distances between tilts. By collecting the particles at the reference angle (0°) which have correctly tracked counterparts at both 30° and −30° from the tracking lists, the particles successfully tracked through all three angles were identified and their 2D coordinates at each angle were recorded as a three-angle tracking list which was used for 3D distance analysis. For the particles which are visible only in two tilt angles, we applied a slightly more strict distance threshold of 5 nm to prepare the final lists of two-angle tracking lists for (0°, 30°), (0°, −30°) and (30°, −30°) angle pairs.

Since tilting the specimen results in substantially varying z positions of the AuNPs, some AuNPs can become out of focus and not visible. This can yield ambiguity in particle tracking, especially when there are two neighboring particles at one angle but one of the particles becomes invisible at other angles. Therefore, we checked if any of the tracked particles had a neighboring untracked particle within 7 nm at each tilt angle, and the particles meeting this criterion were regarded as ambiguous. We removed the 2D coordinates of the ambiguous tracked particles from the list. Because we used a limited distance threshold (7 nm), it was impossible to perfectly remove the 2D coordinates of all ambiguous tracked particles. Therefore, we manually removed the 2D coordinates of tracked particles from the list if any of the following criteria was met:

(i) Two or more particles are gathered too closely around a tracked particle, and the accuracy of tracking cannot be guaranteed.

(ii) The contrasts of some tracked particles were much lower than their neighboring AuNPs, being similar to the background noise level.

We regarded these tracked particles as incorrectly tracked particles and removed their 2D coordinates from the list. The number of tracked AuNPs in three angles and two angles are 1,668 and 6,064, respectively. The number of manually removed tracked particles in three angles and two angles are 670 and 2,312, respectively.

(III) Calculating the 3D positions of particles and the interparticle distance. From the 2D coordinates of tracked AuNPs in tilt series, non-agglomerated AuNPs forming a pair were collected using the criteria used in our previous work[30]: i) There should be only one AuNP (the paired AuNP) within 30 nm for any AuNP forming a pair for every tilt angle, and ii) The distance between the AuNP pair in reference angle should be between 0 nm to 20 nm. Representative cropped images of AuNP pairs are shown in Figure S8, and the numbers of successfully tracked AuNP pairs are summarized in Table S1. For each identified pair of properly tracked AuNPs, 2D coordinates of the AuNPs were fitted using eq S2 to obtain the following four parameters: the z positions of the AuNPs forming a pair ($z_1(\theta_1)$, $z_2(\theta_1)$) and the components of local translation vector (X_n, Y_n), via a least-square algorithm minimizing the squared residue S defined as:

$$S = \sum_{i=1}^{2} \sum_{n=2}^{N} \left(\left(x_{i,calc}(\theta_n) - x_i(\theta_n) \right)^2 + \left(y_{i,calc}(\theta_n) - y_i(\theta_n) \right)^2 \right) \qquad \text{(S3)}$$

where $(x_{i,calc}(\theta_n), y_{i,calc}(\theta_n))$ (i represents the index of tracked particle forming a pair) are the calculated 2D coordinates of the ith particle at angle θ_n using eq S2, and $(x_i(\theta_n), y_i(\theta_n))$ are the 2D coordinates of the tracked AuNP at angle θ_n. N is the number of tilt angles, which is 2 or 3 in our case. Since the unknown z positions of the AuNPs were determined from the fitting, the interparticle distance was directly calculated from the three-dimensional positions of the AuNPs forming a pair. The interparticle distances of all successfully tracked AuNP pairs were calculated and used to plot the interparticle distance distribution.

Supporting Method S6. Fitting interparticle distance distribution using a skewed Gaussian function. The average and width of the interparticle distance distribution were calculated by fitting the distribution using a skewed Gaussian function:

$$f(x) = A\phi\left(\tfrac{x-\mu}{w}\right)\Phi\left(\alpha\left(\tfrac{x-\mu}{w}\right)\right) , \tag{S4}$$

Here, $\phi((x - \mu) / w)$ is a Gaussian function with mean μ and standard deviation w, and $\Phi(\alpha((x - \mu) / w))$ is the cumulative distribution function of $\phi(\alpha(x - \mu) / w)$. α is a parameter indicating skewness, and A is a normalization constant. The parameters α, μ, w and A were used to fit the distribution using the least-square algorithm, and the average and width of the distribution can be obtained from the parameters as:

$$Average = \frac{\int_{-\infty}^{\infty} xf(x)dx}{\int_{-\infty}^{\infty} f(x)dx} , \tag{S5}$$

$$Width = 2w\sqrt{1 - \tfrac{2}{\pi}\left(\tfrac{\alpha}{\sqrt{1+\alpha^2}}\right)^2}. \tag{S6}$$

We estimated the errors of average and width of the interparticle distance distribution by obtaining 100 randomly re-sampled distributions with halved sample size and calculating the standard deviation of the averages and widths of the re-sampled distributions, respectively.

Supporting Method S7. Extracting the inter-residue distance distribution from the MD-generated structures. To compare our experimental measurements of structural changes in CaM upon Aβ25-35 peptide binding with another method, we performed an additional structural analysis based on MD simulations[33]. This analysis consists of two steps: (a) generating candidate structures using MD simulations and (b) calculating the 2-117 Cα-Cα inter-residue distances from the simulated candidate structures. In the first step, MD simulations were conducted for CaM under four different conditions: (i) holo-CaM without Aβ25-35 (holo-CaM), (ii) apo-CaM without Aβ25-35 (apo-CaM), (iii) holo-CaM with Aβ25-35, and (iv) apo-CaM with Aβ25-35. In the second step, we calculated the 2-117 Cα-Cα inter-residue distances of the sampled structures from the MD simulations. The details for the two steps are described below.

MD simulations for holo-CaM and apo-CaM without Aβ25-35. In the simulations, the GROMACS 2019.2 package with the OPLS-AA force field[34] was used in combination with the SPCE (Simple Point Charge Extended) water model. For (i) holo-CaM, we performed the MD simulation using a crystal structure (PDB ID: 1PRW[2]), in which the 2-117 inter-residue distance is shorter than that of the apo-CaM crystal structure, as the MT-NACS data suggest a reduction in the interparticle distance from apo-CaM to holo-CaM. The system was equilibrated under NVT conditions for 100 ps with a velocity-rescale thermostat ($\tau_T = 0.1$ ps, T = 300 K) and was then subsequently equilibrated under NPT conditions for 100 ps with a

velocity-rescale thermostat (τ_T = 0.1 ps, T = 300 K). Afterward, a 200 ns production simulation was conducted. For (ii) apo-CaM, to incorporate the relatively broader interparticle distance distribution of apo-CaM (which suggests multiple conformational states of compact and flexible structures within the distribution), the MD simulations were started from four different structures reported for apo-CaM (PDB ID: 6BUT, 2N8J, 1DMO, 4LZX)[10, 35-37] as the starting conformations and the simulations were performed similarly as for (i). After the simulation, the candidate structures for (i) and (ii) were sampled at 1 ps intervals from the MD trajectories. From the MD trajectories, the representative structures of (i) and (ii) were selected by using the clustering method and were used to construct the starting structures for the simulations of (iii) and (iv), respectively.

MD simulations for holo-CaM and apo-CaM with Aβ25-35. Prior to the MD simulations for (iii) and (iv), we performed the docking simulation to construct complex conformations of holo-CaM with Aβ25-35 and apo-CaM with Aβ25-35 from the representative structures. The simulations were achieved by the CABS-dock web server (http://biocomp.chem.uw.edu.pl/CABSdock/)[40] as follows. In each docking simulation, the CABS-dock simulation generated the top 10 predicted models which evaluate probable protein-peptide sites. Among the predicted models, the models with the highest scores were considered as the most reasonable conformations for holo-CaM with Aβ25-35 and apo-CaM with Aβ25-35, respectively. We used these complex conformations as the starting structures of the MD simulations for (iii) and (iv), and the MD simulations were performed as described above for the simulation for (i). After the simulations, the candidate structures for (iii) and (iv) were sampled at 1 ps intervals from the MD trajectories.

Calculating the 2-117 Cα-Cα inter-residue distances of CaM with and without Aβ25-35 peptide. The inter-residue distance distributions for CaM were calculated from the candidate structures. After the calculation, we plotted the distances of (i) and (iii) as histograms to construct the inter-residue distance distributions of holo-CaM with and without Aβ25-35 (Figure 5d). For the construction of the inter-residue distance distributions of apo-CaM with and without Aβ25-35, we merged the distances of 4 different structures of (ii) and (iv) for the histogram plots (Figure 5c).

Supporting Method S8. Extraction of the inter-fluorophore distance from FRET and smFRET data. In some smFRET studies, inter-fluorophore distances were not reported and only FRET efficiency distributions were reported. We used the following equation connecting the FRET efficiency and donor-acceptor distance within a point dipole-dipole approximation to calculate the inter-fluorophore distance[38].

$$\text{FRET efficiency} = \frac{1}{1+\left(\frac{r}{R_0}\right)^6} \tag{S7}$$

Here, r is the inter-fluorophore distance, and R_0 is the inter-fluorophore distance when the FRET efficiency is 50%. Using the reported distribution of FRET efficiency, the distance distribution was extracted and then fitted using the Gaussian function to determine the peak position (as the average) and the width.

Supporting Method S9. Extracting the radii of gyration and inter-residue distances from NMR structures. As the labeling positions employed in FRET and smFRET studies differ slightly from those used in our work using MT-NACS, we investigated the relationship

between different inter-residue distances. For this purpose, we used previously reported NMR structures containing an ensemble of 25 structures for apo-CaM (PDB: 1CFC)[9] and an ensemble of 20 structures for holo-CaM (PDB: 1X02)[11]. For this analysis, we picked four different inter-residue distances: the 2-117 pair, which is the one used for our MT-NACS work, and 17-117, 34-110, and 69-99 pairs, which were used in FRET and smFRET studies[14-16]. The Cα-Cα distance was taken to represent the corresponding inter-residue distance. Our analysis revealed that the inter-residue distances exhibit positive correlations with one another (Figure S9). We also examined the relationship between the inter-residue distances and the radius of gyration (R_g). Our analysis indicated positive correlations between inter-residue distances and R_g values (Figure S10), suggesting that a reduction in inter-residue distance is typically associated with an overall contraction of the protein structure, and vice versa. Of course, it should be noted that the correlation between R_g value and inter-residue distance is not absolute, as there are instances where an increase in R_g value may be accompanied by a decrease in inter-residue distance. It is of note that in both Figure S9 and Figure S10, holo-CaM shows weaker correlations than apo-CaM.

Supporting References

(1) Schumacher, M. A.; Crum, M.; Miller, M. C. Crystal structures of apocalmodulin and an apocalmodulin/SK potassium channel gating domain complex. *Structure* **2004**, *12*, 849-860.

(2) Fallon, J. L.; Quiocho, F. A. A closed compact structure of native Ca^{2+}-calmodulin. *Structure* **2003**, *11*, 1303-1307.

(3) Babu, Y. S.; Bugg, C. E.; Cook, W. J. Structure of calmodulin refined at 2.2 Å resolution. *J. Mol. Biol.* **1988**, *204*, 191-204.

(4) Taylor, D. A.; Sack, J. S.; Maune, J. F.; Beckingham, K.; Quiocho, F. A. Structure of a recombinant calmodulin from Drosophila melanogaster refined at 2.2-Å resolution. *J. Biol. Chem.* **1991**, *266*, 21375-21380.

(5) Ban, C.; Ramakrishnan, B.; Ling, K. Y.; Kung, C.; Sundaralingam, M. Structure of the recombinant Paramecium tetraurelia calmodulin at 1.68 Å resolution. *Acta Crystallogr. D Biol. Crystallogr.* **1994**, *50*, 50-63.

(6) Chattopadhyaya, R.; Meador, W. E.; Means, A. R.; Quiocho, F. A. Calmodulin structure refined at 1.7 Å resolution. *J. Mol. Biol.* **1992**, *228*, 1177-1192.

(7) Rao, S. T.; Wu, S.; Satyshur, K. A.; Ling, K. Y.; Kung, C.; Sundaralingam, M. Structure of Paramecium tetraurelia calmodulin at 1.8 Å resolution. *Protein Sci.* **1993**, *2*, 436-447.

(8) Wilson, M. A.; Brunger, A. T. The 1.0 Å crystal structure of Ca^{2+}-bound calmodulin: an analysis of disorder and implications for functionally relevant plasticity. *J. Mol. Biol.* **2000**, *301*, 1237-1256.

(9) Kuboniwa, H.; Tjandra, N.; Grzesiek, S.; Ren, H.; Klee, C. B.; Bax, A. Solution structure of calcium-free calmodulin. *Nat. Struct. Biol.* **1995**, *2*, 768-776.

(10) Zhang, M.; Tanaka, T.; Ikura, M. Calcium-induced conformational transition revealed by the solution structure of apo calmodulin. *Nat. Struct. Biol.* **1995**, *2*, 758-767.

(11) Kainosho, M.; Torizawa, T.; Iwashita, Y.; Terauchi, T.; Mei Ono, A.; Guntert, P. Optimal isotope labelling for NMR protein structure determinations. *Nature* **2006**, *440*, 52-57.

(12) Gsponer, J.; Christodoulou, J.; Cavalli, A.; Bui, J. M.; Richter, B.; Dobson, C. M.; Vendruscolo, M. A coupled equilibrium shift mechanism in calmodulin-mediated signal transduction. *Structure* **2008**, *16*, 736-746.

(13) Yao, Y.; Schoneich, C.; Squier, T. C. Resolution of structural changes associated with calcium activation of calmodulin using frequency domain fluorescence spectroscopy. *Biochemistry* **1994**, *33*, 7797-7810.

(14) Sun, H.; Yin, D.; Squier, T. C. Calcium-dependent structural coupling between opposing globular domains of calmodulin involves the central helix. *Biochemistry* **1999**, *38*, 12266-12279.

(15) Torok, K.; Tzortzopoulos, A.; Grabarek, Z.; Best, S. L.; Thorogate, R. Dual effect of ATP in the activation mechanism of brain Ca^{2+}/calmodulin-dependent protein kinase II by Ca^{2+}/calmodulin. *Biochemistry* **2001**, *40*, 14878-14890.

(16) Hellstrand, E.; Kukora, S.; Shuman, C. F.; Steenbergen, S.; Thulin, E.; Kohli, A.; Krouse, B.; Linse, S.; Akerfeldt, K. S. Forster resonance energy transfer studies of calmodulin produced by native protein ligation reveal inter-domain electrostatic repulsion. *FEBS J.* **2013**, *280*, 2675-2687.

(17) DeVore, M. S.; Braimah, A.; Benson, D. R.; Johnson, C. K. Single-Molecule FRET States, Conformational Interchange, and Conformational Selection by Dye Labels in Calmodulin. *J. Phys. Chem. B* **2016**, *120*, 4357-4364.

(18) McCarthy, M. R.; Savich, Y.; Cornea, R. L.; Thomas, D. D. Resolved Structural States of Calmodulin in Regulation of Skeletal Muscle Calcium Release. *Biophys. J.* **2020**, *118*, 1090-1100.

(19) Slaughter, B. D.; Allen, M. W.; Unruh, J. R.; Bieber Urbauer, R. J.; Johnson, C. K. Single-Molecule Resonance Energy Transfer and Fluorescence Correlation Spectroscopy of Calmodulin in Solution. *J. Phys. Chem. B* **2004**, *108*, 10388–10397.

(20) Slaughter, B. D.; Unruh, J. R.; Allen, M. W.; Bieber Urbauer, R. J.; Johnson, C. K. Conformational substates of calmodulin revealed by single-pair fluorescence resonance energy transfer: influence of solution conditions and oxidative modification. *Biochemistry* **2005**, *44*, 3694-3707.

(21) Devore, M. S.; Gull, S. F.; Johnson, C. K. Reconstruction of Calmodulin Single-Molecule FRET States, Dye-Interactions, and CaMKII Peptide Binding by MultiNest and Classic Maximum Entropy. *Chem. Phys.* **2013**, *422*, 238-245.

(22) Han, M. J.; He, Q. T.; Yang, M.; Chen, C.; Yao, Y.; Liu, X.; Wang, Y.; Zhu, Z. L.; Zhu, K. K.; Qu, C.; Yang, F.; Hu, C.; Guo, X.; Zhang, D.; Chen, C.; Sun, J. P.; Wang, J. Single-molecule FRET and conformational analysis of beta-arrestin-1 through genetic code expansion and a Se-click reaction. *Chem. Sci.* **2021**, *12*, 9114-9123.

(23) Sadoine, M.; Cerminara, M.; Kempf, N.; Gerrits, M.; Fitter, J.; Katranidis, A. Selective Double-Labeling of Cell-Free Synthesized Proteins for More Accurate smFRET Studies. *Anal. Chem.* **2017**, *89*, 11278-11285.

(24) Anthis, N. J.; Doucleff, M.; Clore, G. M. Transient, sparsely populated compact states of apo and calcium-loaded calmodulin probed by paramagnetic relaxation enhancement: interplay of conformational selection and induced fit. *J. Am. Chem. Soc.* **2011,** *133*, 18966-18974.

(25) Pandey, K.; Dhoke, R. R.; Rathore, Y. S.; Nath, S. K.; Verma, N.; Bawa, S.; Ashish. Low pH overrides the need of calcium ions for the shape-function relationship of calmodulin: resolving prevailing debates. *J. Phys. Chem. B* **2014,** *118*, 5059-5074.

(26) Bayley, P.; Martin, S.; Jones, G. The conformation of calmodulin: a substantial environmentally sensitive helical transition in Ca_4-calmodulin with potential mechanistic function. *FEBS Lett.* **1988,** *238*, 61-66.

(27) Bayley, P. M.; Martin, S. R. The alpha-helical content of calmodulin is increased by solution conditions favouring protein crystallisation. *Biochim. Biophys. Acta* **1992,** *1160*, 16-21.

(28) Minnes, L.; Greetham, G. M.; Shaw, D. J.; Clark, I. P.; Fritzsch, R.; Towrie, M.; Parker, A. W.; Henry, A. J.; Taylor, R. J.; Hunt, N. T. Uncovering the Early Stages of Domain Melting in Calmodulin with Ultrafast Temperature-Jump Infrared Spectroscopy. *J. Phys. Chem. B* **2019,** *123*, 8733-8739.

(29) Grant, B. M. M.; Marshall, C. B.; Ikura, M. Expression and Purification of Calmodulin for NMR and Other Biophysical Applications. *Methods Mol. Biol.* **2019**, *1929*, 207-221.

(30) Ki, H.; Jo, J.; Kim, Y.; Kim, T. W.; Kim, C.; Kim, Y.; Kim, C. W.; Muniyappan, S.; Lee, S. J.; Kim, Y.; Kim, H. M.; Yang, Y.; Ihee, H. Uncovering the Conformational Distribution of a Small Protein with Nanoparticle-Aided Cryo-Electron Microscopy Sampling. *J. Phys. Chem. Lett.* **2021**, *12*, 6565-6573.

(31) Blair, D.; Dufresne, E. The Matlab Particle Tracking Code Repository https://site.physics.georgetown.edu/matlab (2005).

(32) Xu, R.; Chen, C. C.; Wu, L.; Scott, M. C.; Theis, W.; Ophus, C.; Bartels, M.; Yang, Y.; Ramezani-Dakhel, H.; Sawaya, M. R.; Heinz, H.; Marks, L. D.; Ercius, P.; Miao, J. Three-

dimensional coordinates of individual atoms in materials revealed by electron tomography. *Nat. Mater.* **2015**, *14*, 1099-1103.

(33) Van Der Spoel, D.; Lindahl, E.; Hess, B.; Groenhof, G.; Mark, A. E.; Berendsen, H. J. GROMACS: fast, flexible, and free. *J. Comput. Chem.* **2005,** *26*, 1701-1718.

(34) Robertson, M. J.; Tirado-Rives, J.; Jorgensen, W. L. Improved Peptide and Protein Torsional Energetics with the OPLSAA Force Field. *J. Chem. Theory Comput.* **2015**, *11*, 3499-3509.

(35) Chen, L. T.; Liang, W. X.; Chen, S.; Li, R. K.; Tan, J. L.; Xu, P. F.; Luo, L. F.; Wang, L.; Yu, S. H.; Meng, G.; Li, K. K.; Liu, T. X.; Chen, Z.; Chen, S. J. Functional and molecular features of the calmodulin-interacting protein IQCG required for haematopoiesis in zebrafish. *Nat. Commun.* **2014**, *5*, 3811.

(36) Mahling, R.; Hovey, L.; Isbell, H. M.; Marx, D. C.; Miller, M. S.; Kilpatrick, A. M.; Weaver, L. D.; Yoder, J. B.; Kim, E. H.; Andresen, C. N. J.; Li, S.; Shea, M. A. $Na_V1.2$ EFL domain allosterically enhances Ca^{2+} binding to sites I and II of WT and pathogenic calmodulin mutants bound to the channel CTD. *Structure* **2021**, *29*, 1339-1356.

(37) Piazza, M.; Dieckmann, T.; Guillemette, J. G. Structural Studies of a Complex Between Endothelial Nitric Oxide Synthase and Calmodulin at Physiological Calcium Concentration. *Biochemistry* **2016**, *55*, 5962-5971.

(38) Stryer, L. Fluorescence Energy Transfer as a Spectroscopic Ruler. *Annu. Rev. Biochem.* **1978**, *47*, 819–846.

(39) Hellstrand, E.; Kukora, S.; Shuman, C. F.; Steenbergen, S.; Thulin, E.; Kohli, A.; Krouse, B.; Linse, S.; Akerfeldt, K. S. Forster resonance energy transfer studies of calmodulin produced by native protein ligation reveal inter-domain electrostatic repulsion. *FEBS J.* **2013**, *280*, 2675-2687.

(40) Kurcinski, M.; Jamroz, M.; Blaszczyk, M.; Kolinski, A.; Kmiecik, S. CABS-dock web server for the flexible docking of peptides to proteins without prior knowledge of the binding site. *Nucleic Acids Res.* **2015,** *43*, W419-424.

Supporting Table

Table S1. Numbers of successfully tracked AuNP pairs found for various experimental conditions.

Experimental condition	Total number of successfully tracked pairs	Number of successfully tracked pairs in three angles	Number of successfully tracked pairs only in two angles
Apo-CaM with NaCl 150 mM	109	39	70
Holo-CaM with NaCl 150 mM	111	45	66
Apo-CaM with NaCl 50 mM	100	43	57
Holo-CaM with NaCl 50 mM	112	65	47
Apo-CaM + Aβ25-35 with NaCl 150 mM	116	83	33
Holo-CaM + Aβ25-35 with NaCl 150 mM	101	31	70

Supporting Figures

a

b

c
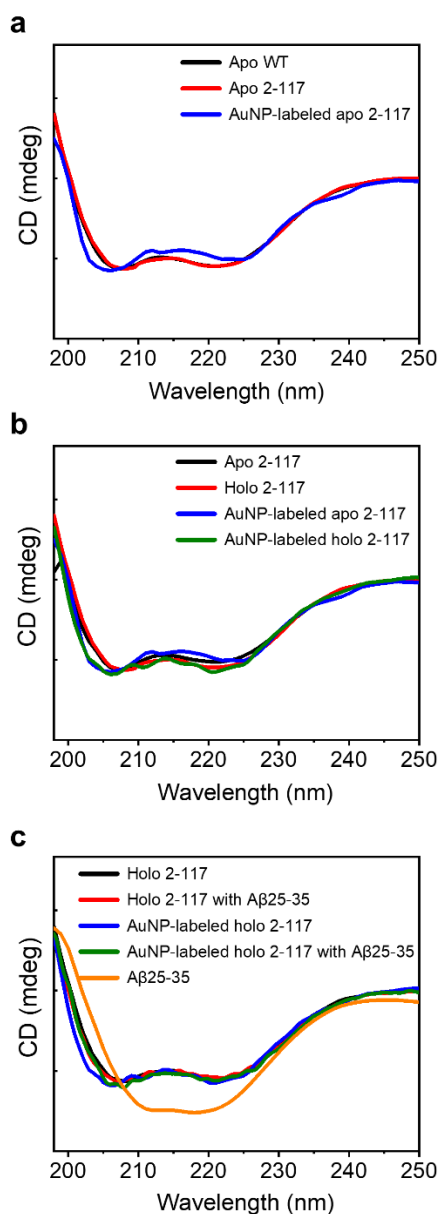
Figure S1. Results of CD measurement. (a) CD spectra of apo-CaM wild type (WT) (black), apo-CaM 2-117 (red) and AuNP-labeled apo-CaM 2-117 (blue). (b) CD spectra of apo-CaM 2-117 (black), holo-CaM 2-117 (red), AuNP-labeled apo-CaM 2-117 (blue) and AuNP-labeled holo-CaM 2-117 (green). (c) CD spectra of holo-CaM 2-117 (black), holo-CaM 2-117 bound with Aβ25-35 (red), AuNP-labeled holo-CaM 2-117 (blue), AuNP-labeled holo-CaM 2-117 bound with Aβ25-35 (green) and Aβ25-35 (orange).
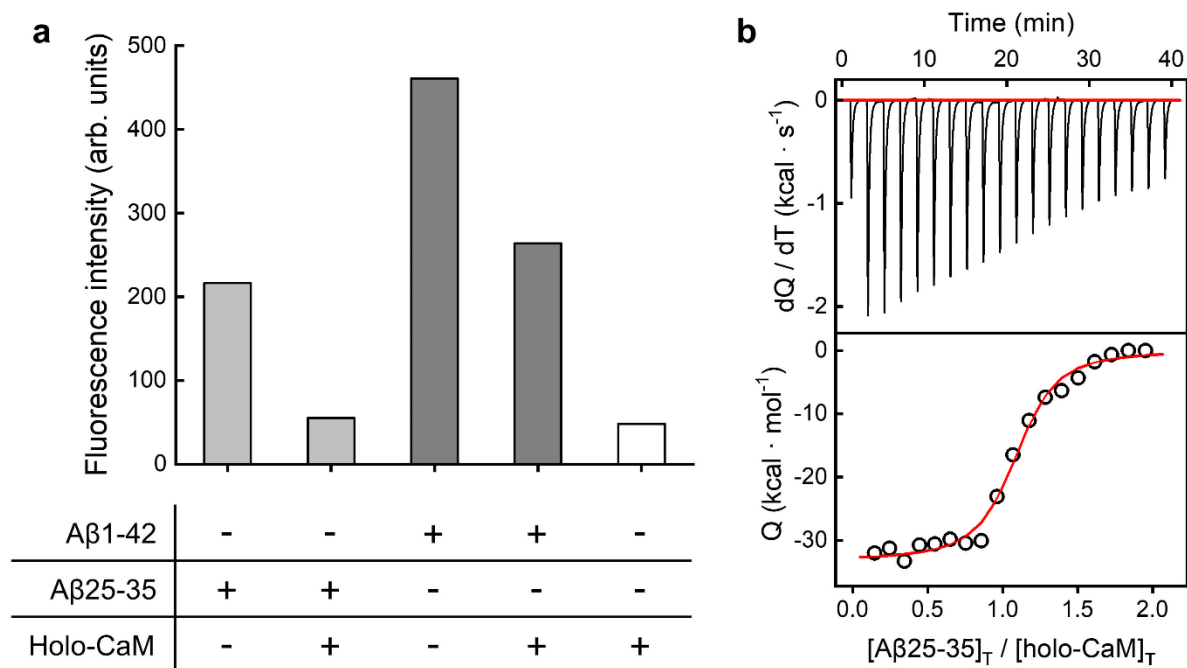
Figure S2. Characterization of holo-CaM and Aβ25-35. (a) ThT aggregation assay for CaM and Aβ peptides. The bar graphs correspond to Aβ25-35, holo-CaM with Aβ25-35, Aβ1-42, holo-CaM with Aβ1-42, and holo-CaM from left to right. (b) ITC profile for CaM and Aβ25-35. (Top) Calorimetric titration profile for injection of Aβ25-35 into holo-CaM. (Bottom) Incremental enthalpy changes with experimental points (black circles) and the best fitting result (solid red line). Data were fitted using a one-site binding model.
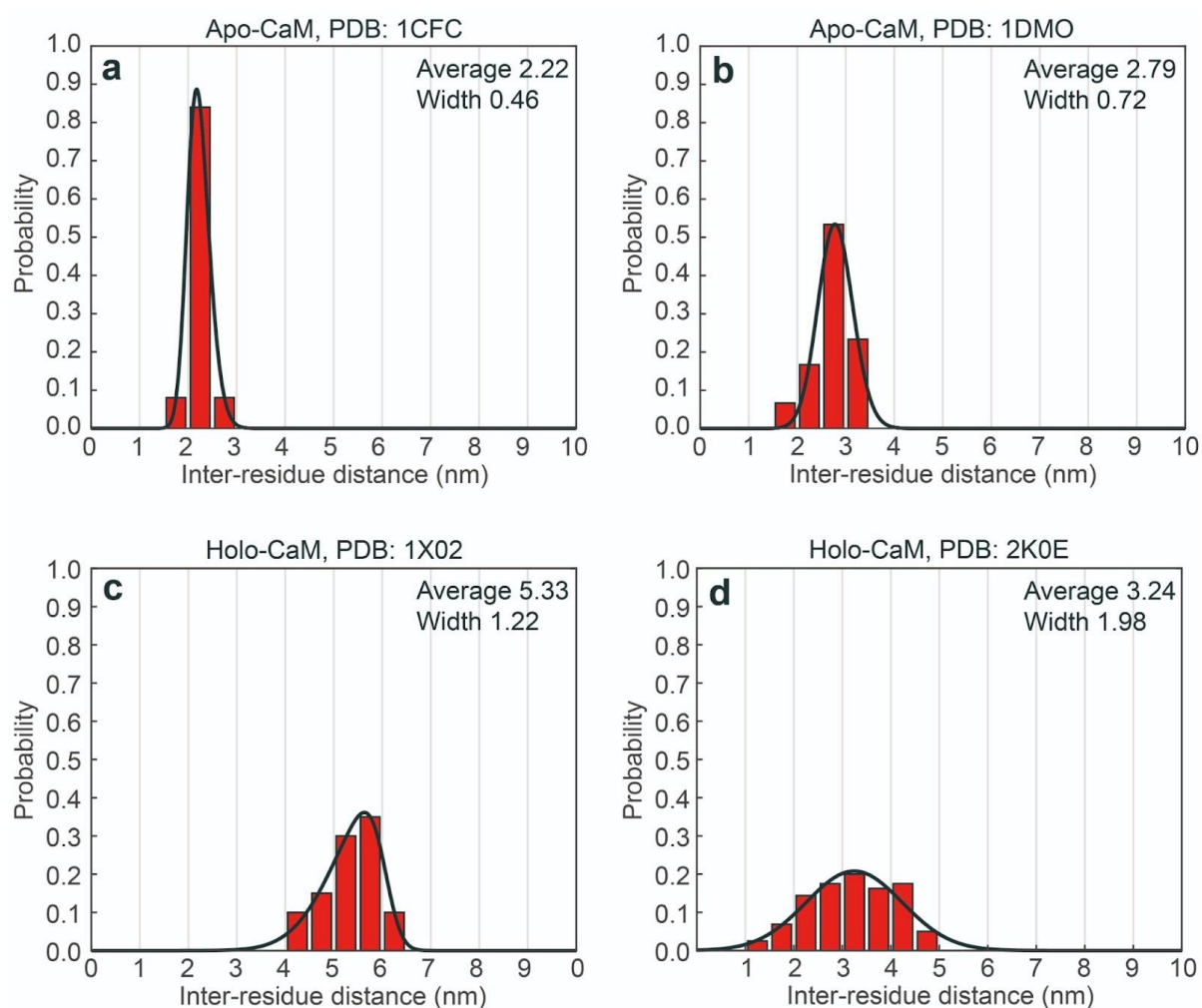
Figure S3. Inter-residue distance distributions of CaM based on reported NMR structures. The distances between the 2nd and 117th residues, which are the positions used in our MT-NACS experiments, were extracted from the ensemble structures from previously reported NMR studies. The black lines represent the fitted interparticle distance distributions using a skewed Gaussian function. The unit of average and width is nm. (a, b) Apo-CaM. (c, d) Holo-CaM.
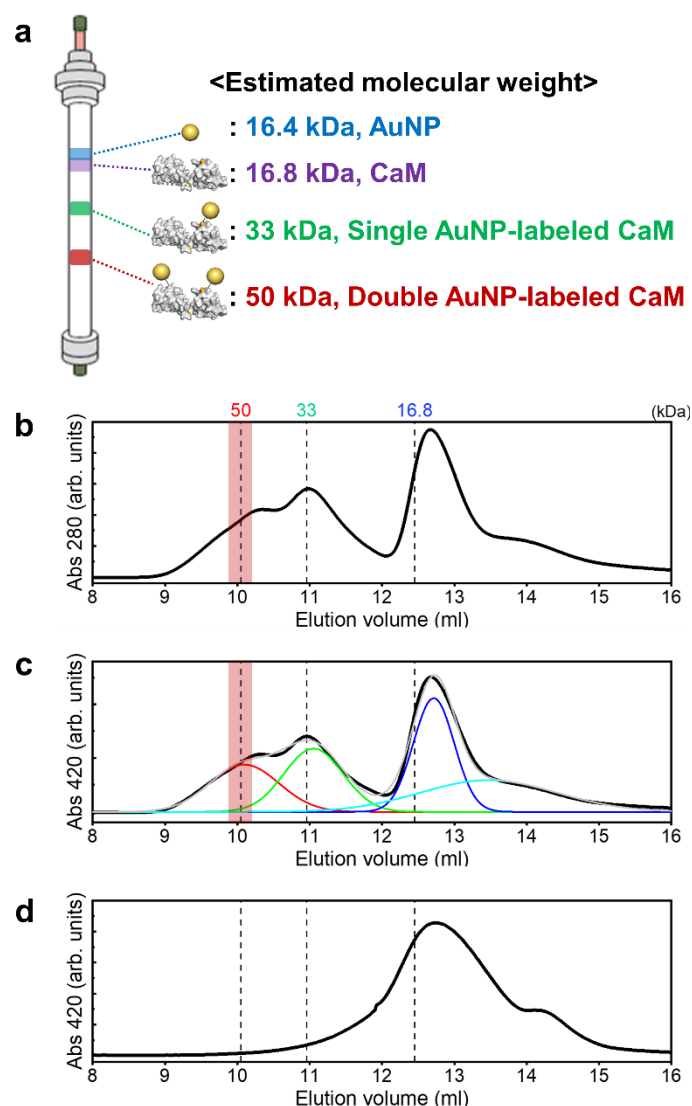
Figure S4. SEC result of AuNP-labeled CaM. (a) (left) Schematic diagram for isolating CaM labeled with two AuNPs using the SEC column. (right) The estimated molecular weight of the molecules in the mixture; a single AuNP (blue), unlabeled CaM (purple), CaM labeled with a single AuNP (green), and CaM labeled with two AuNPs (red). (b) Elution profile at 280 nm of the reaction mixture for labeling AuNPs to CaM. (c) Elution profile at 420 nm, where only AuNPs can absorb, of the reaction mixture for labeling AuNPs to CaM. The elution profile (black) can be decomposed into four peaks, and their sum (grey) reproduces the elution profile well. The first peak (red) and the second peak (green) are assigned to CaM labeled with two

AuNPs and CaM labeled with one AuNP, respectively, while the remaining two peaks (blue and cyan) are attributed to unlabeled AuNPs. In (b) and (c), the center portion used to prepare the cryo-EM samples for the MT-NACS experiment is highlighted with a vertical red bar. (d) Elution profile at 420 nm, where only AuNPs can absorb, of a control solution containing only AuNPs without CaM. The two peaks assigned to CaM labeled with one or two AuNPs in (c) are missing in (d).
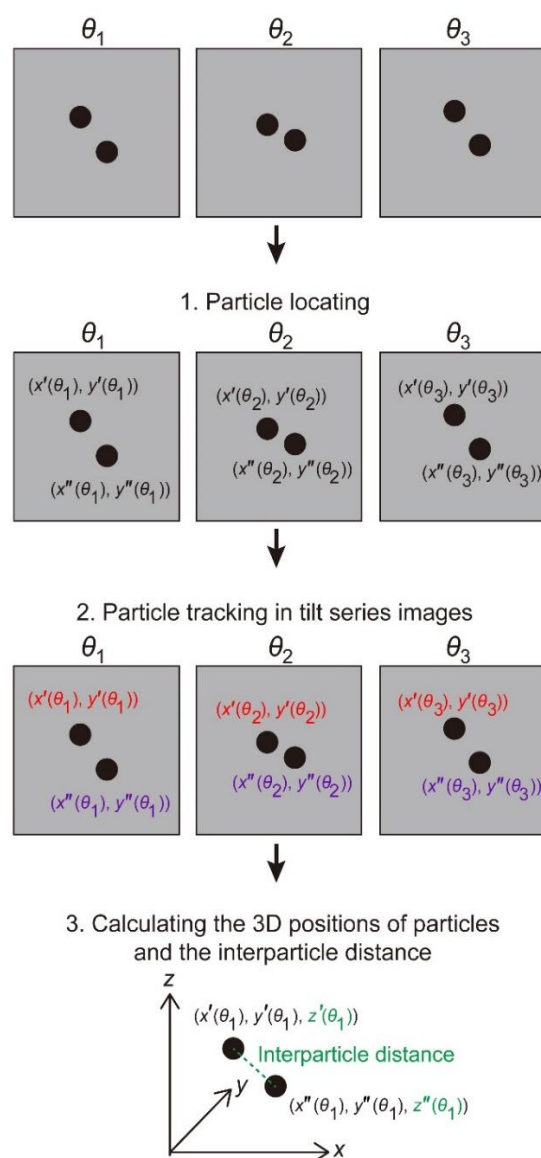
Figure S5. Schematic diagram of calculating the interparticle distances of AuNP-labeled proteins. In the first step (particle locating), the 2D coordinates of the particles in the tilt series images were obtained, and in the second step (particle tracking in tilt series images), the same particles at different tilt angles were tracked. The 2D coordinates of the same particles are marked in the same color (red and purple). In the third step (calculating the 3D positions of particles and the interparticle distance), the z positions of particles (Green) at the reference angle θ_1 were obtained by least-square fittings based on the 2D coordinates of tracked particles, and the interparticle distance was finally calculated.
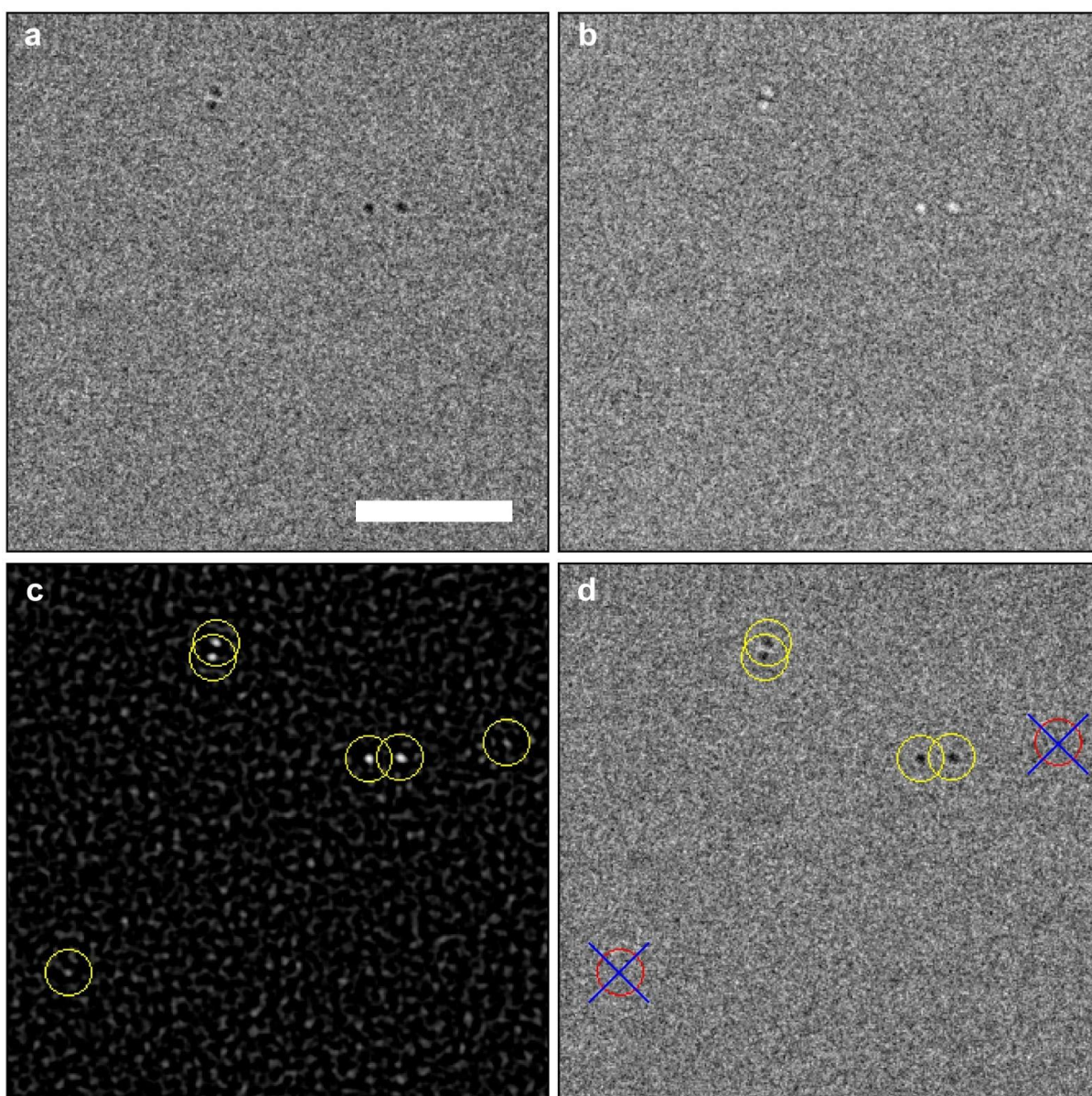
Figure S6. Example of the particle locating process. (a) Representative image after 4 × 4 binning and normalization. (b) Contrast inverted image of (a). (c) The image after post-processing. Yellow circles indicate the identified local maxima pixels. (d) Image (a) with the identified local maxima pixels marked. Local maxima pixels originating from AuNPs and background noise are indicated by yellow circles and red circles with blue cross marks, respectively. Scale bar: 30 nm.
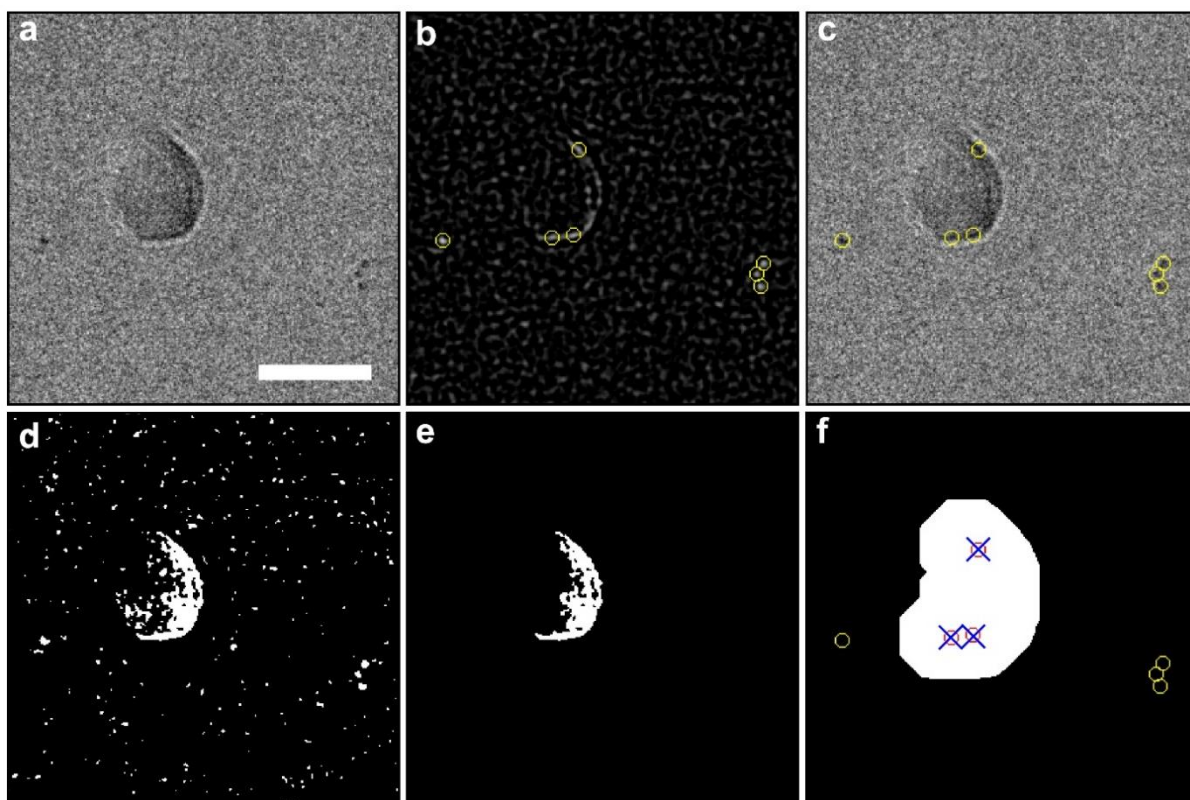
Figure S7. Excluding artifacts due to crystal ice. (a) Representative cryo-EM image that contains a crystal ice flake. (b) Post-processed image where identified local maxima pixels are indicated by yellow circles. (c) Image (a) with the identified local maxima pixels marked with yellow circles. (d–f) Processes of removing artifacts due to crystal ice boundary. An intensity threshold was applied to create a binary mask image (d) followed by area thresholding to separate only the crystal ice boundary (e). To fully enclose the crystal ice boundary region inside the mask, we expanded the mask using the MATLAB built-in function 'imdilate' (f). Local maxima pixels originating from AuNPs and the crystal ice flake are indicated by yellow circles and red circles with blue cross marks, respectively. Scale bar: 30 nm.
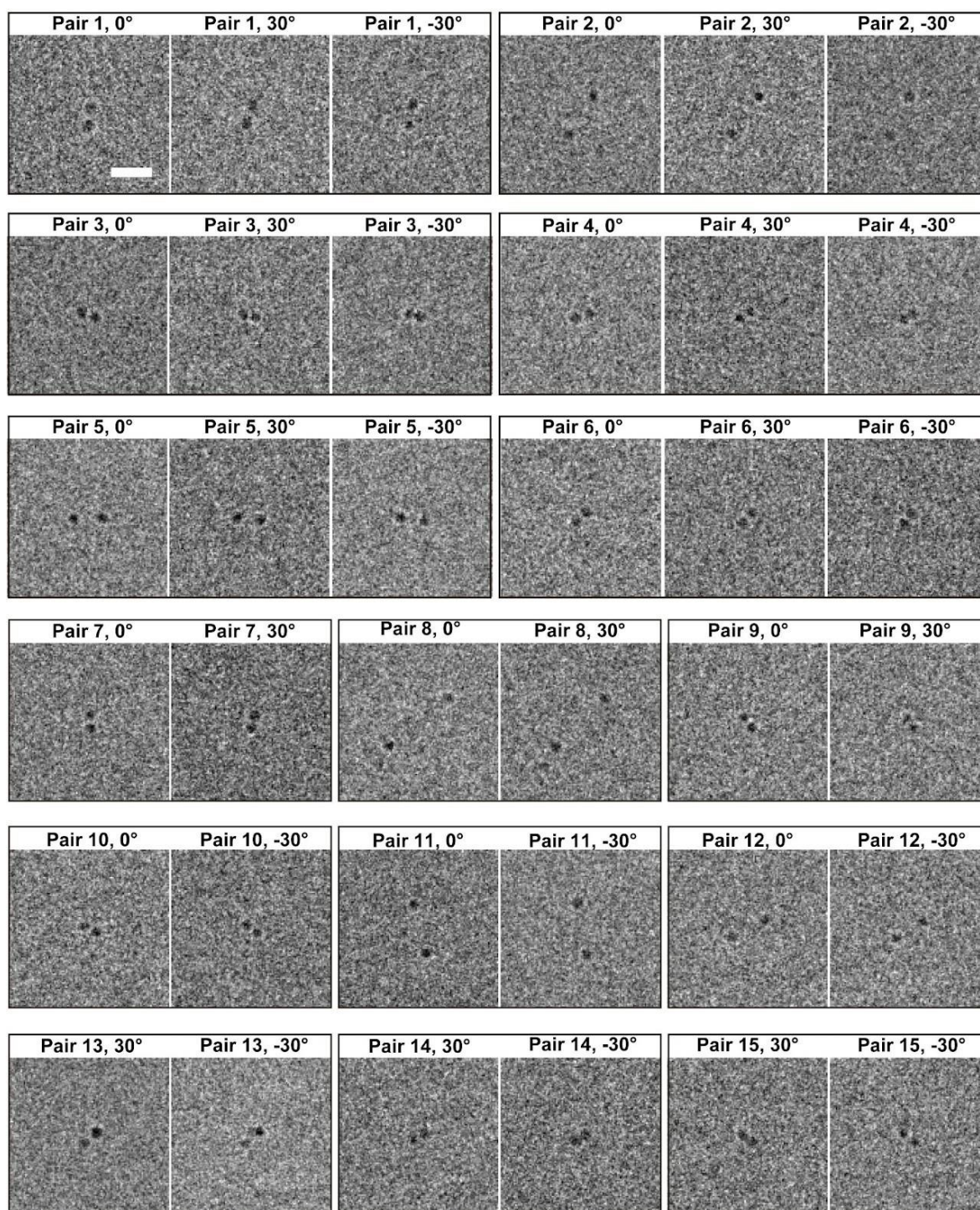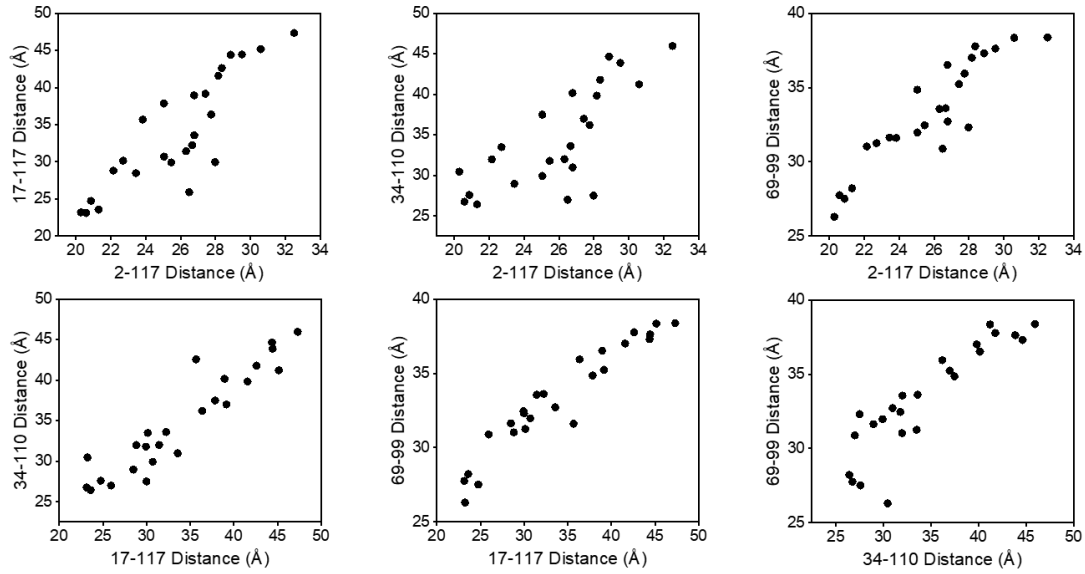
Figure S8. Representative cropped images of AuNP-labeled apo-CaM under the 150 mM NaCl condition. 15 representative AuNP pairs (6 pairs tracked in three angles, 9 pairs tracked only for two angles) are selected from 109 successfully tracked AuNP pairs and plotted. Scale bar: 10 nm.
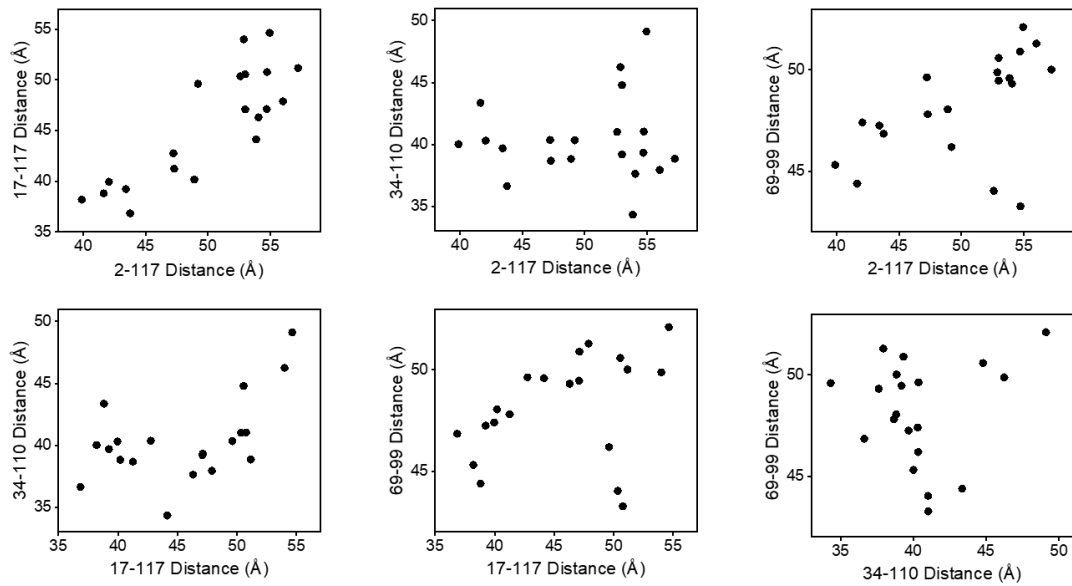
Figure S9. Correlations between various inter-residue distances observed in reported NMR structures. The ensemble for apo-CaM (PDB: 1CFC) has 25 structures, and that for holo-CaM (PDB: 1X02) has 20 structures. Four different inter-residue distances (2-117 pair used for MT-NACS, and 17-117, 34-110, and 69-99 pairs, which were used in FRET and smFRET studies) were inspected. The Cα-Cα distance was taken to represent the corresponding inter-residue distance.
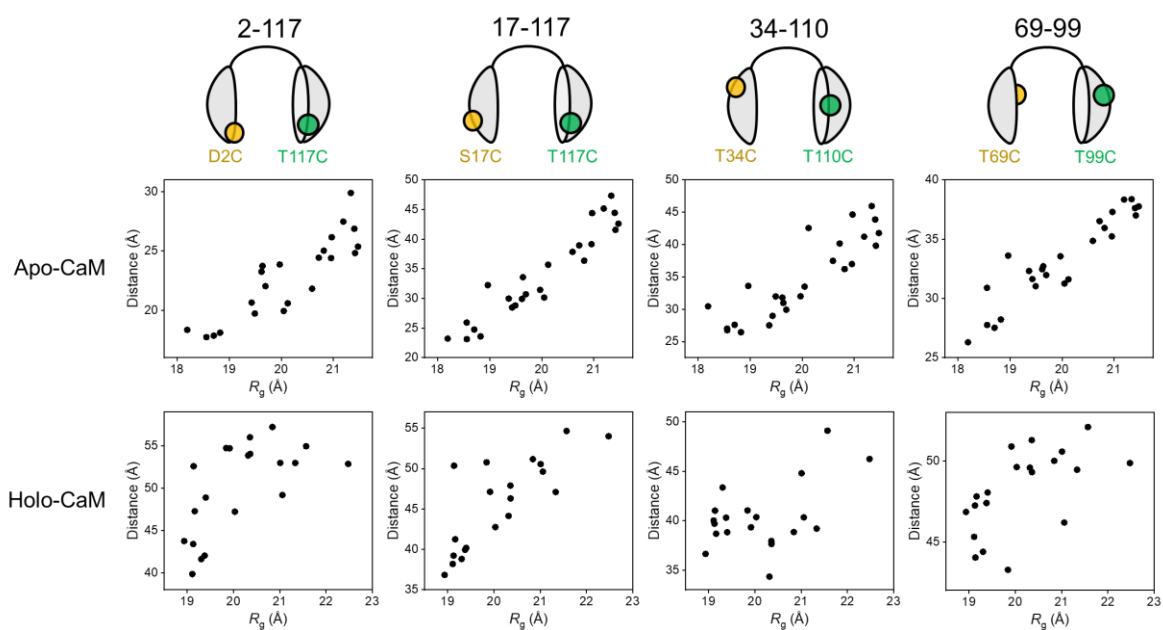
Figure S10. Correlations between various inter-residue distances and R_g observed in reported NMR structures. The ensemble for apo-CaM (PDB: 1CFC) has 25 structures, and that for holo-CaM (PDB: 1X02) has 20 structures. Four different inter-residue distances (2-117 pair used for MT-NACS, and 17-117, 34-110, and 69-99 pairs, which were used in FRET and smFRET studies) were inspected. The Cα-Cα distance was taken to represent the corresponding inter-residue distance.